Bifocal Optical-Vortex Lens with Sorting of the Generated Nonseparable Spin-Orbital Angular-Momentum States

Alwin M. W. Tam,[1,*] Fan Fan,[2,†] Tao Du,[1] Wei Hu,[3] Wanlong Zhang,[1] Chenxiang Zhao,[1] Xiaoqian Wang,[1] Kwong-Lung Ching,[1] Guijun Li,[1] Hailu Luo,[2] Vladimir G. Chigrinov,[1] Shuangchun Wen,[2] and Hoi-Sing Kwok[1]

[1]*Partner State Key Laboratory (PSKL) on Advanced Displays and Optoelectronics Technologies, Department of Electronic and Computer Engineering, Hong Kong University of Science and Technology, Clear Water Bay, Kowloon 999077, Hong Kong*

[2]*Key Laboratory for Micro-/Nano- Optoelectronic Devices of Ministry of Education, School of Physics and Electronics, Hunan University, Changsha 410082, China*

[3]*National Laboratory of Solid State Microstructures and College of Engineering and Applied Sciences, Nanjing University, Nanjing 210093, China*

(Received 9 December 2016; published 17 March 2017)

In this article, we devise and demonstrate experimentally a polarization-dependent diffractive bifocal vortex lens operating via the Pancharatnam-Berry phase. The interaction between the incident beam and the bifocal vortex lens establishes nonseparable spin and orbital angular-momentum photon states. The components of the nonseparable state associated with different couplings of spin and orbital angular momentum can be sorted by the bifocality of the lens. A theoretical model of the device is developed using Fresnel's diffraction. The device is simply, efficiently, and economically realized from the optical setup using the underlying physics of Pancharatnam-Berry-phase polarization holography. The measured transmittance and diffraction efficiency of the fabricated device is high—up to 90% and 91%, respectively. Various applications of the polarization bifocal vortex lens in the field of orbital angular-momentum lasing and optical manipulation are discussed. Thus, the bifocal vortex lens can have significant impact on classical and quantum optics, as well as theoretical physics.

DOI: 10.1103/PhysRevApplied.7.034010

I. INTRODUCTION

Recently, there has been an ever-growing interest in the study and manipulation of the angular momentum of light. It can be classified into two distinct components, the intrinsic spin angular momentum (SAM) and the orbital angular momentum (OAM) [1]. The SAM is associated with the polarization state forming a Hilbert space that consists of two orthogonal states. Each left-handed circularly (LHC) or right-handed circularly (RHC) polarized photon carrying a quantized spin of $-$ or $+\hbar$ respectively, corresponds to an orthogonal state [2]. The OAM is associated with the twistedlike helical wave front with a phase singularity at the beam axis. The helical beam is known as the optical vortex, which has a distinctive annular ring intensity profile with a dark region at the center due to the presence of phase singularity [3] [refer to Fig. 3(d) for an illustration]. The electric field of a vortex beam is dependent on the azimuth angle φ, i.e., $\boldsymbol{E}(r,\varphi) \propto \exp(im\varphi)$. As a result, the OAM establishes a Hilbert space with an unbounded integer m representing an orthogonal state, and each photon in the mth mode carries an OAM of $\pm m\hbar$, where the sign denotes the handedness of the twisted wave front [1]. The unique annular intensity profile and the nature of the OAM of the vortex beam has found many applications in the realm of classical and quantum optics including astronomical observations [4], nanofabrication [5], optical communication systems [6–10], optical trapping [11–13], biological studies [14], quantum-state manipulation of cold atoms [15], and optically driven rotors [16].

Nevertheless, the recent successes of various applications of the optical vortex are intimately connected to the generation and the sorting of the vortex beam. The vortex beam can be generated indirectly by mode conversion using a cylindrical lens [1] or directly from diffractive optical elements using a spiral phase plate [17]. More recently, Marrucci *et al.* [18] developed a special birefringent wave plate known as a q plate that generates a vortex beam of $+2Q$ or $-2Q$ depending on the handedness of the circular polarization of the incident beam [18]. Shortly after, forked polarization grating (FPG) was developed for the generation of vortex beams with many different modes [19,20]. Work has been conducted on the sorting of different OAM modes of the vortex beam using an interferometric approach [21] and optical geometrical transformation [22,23]. However, the aforementioned OAM sorters in Refs. [21–23] do not simultaneously exhibit the property of behaving as an OAM generator.

*amwtam@connect.ust.hk
†eeffan@163.com

The lens is an indispensable tool in a practical vortex system for controlling the size of the generated vortex beam at certain spatial points of interest [6–16]. These systems typically possess only one focal point. However, the limitation of a single-focus vortex system is apparent. For example, it is difficult for a single-focus vortex system to spatially distinguish the generated vortex beams with different OAM, which is crucial for the realization of a laser cavity to generate a coherent beam with definite helical modes (refer to Sec. V C for details). Moreover, it is possible to establish an "optical-twist" effect for particles that are optically trapped in a bifocal vortex system, which can be useful for testing mechanical properties for biological and molecular samples (refer to Sec. V B for details).

To resolve the existing problems of a single-focus vortex system, in this article, we propose a dielectric thin-film Pancharatnam-Berry-phase optical-vortex lens (PBOVL) that has the capability of generating two focal points with different OAM. A close-form solution that sufficiently describes the characteristics of the proposed device is derived from the theoretical model using Fresnel-Kirchoff diffraction theory. We highlight that the device can be simply, efficiently, and economically realized using our PB-phase hologram setup. The proposed multifocal optical-vortex generator with sorting of OAM modes resolves the existing limitations of the conventional single-focus system, which stimulates discoveries for the applications of the optical vortex in the realm of classical and quantum optics.

II. THEORETICAL ANALYSES

Similar to other PB-phase optical elements (PBOEs), such as the q plate and FPG, the PBOVL is a flat optical element that features a spatially variant optical axis that is adopted to establish a PB-phase profile for controlling the wave front of incident light [18,20]. Its optics axis on the incident plane of the PBOVL is expressed as

$$\alpha(r,\varphi) = Q\varphi + \frac{\pi}{2f\lambda}r^2 + \alpha_0, \tag{1}$$

where Q is the topological charge, f is the focal length, λ is the wavelength of the incident light, r is the radial distance, and α_0 is a constant.

To analyze the optical properties of the PBOVL, it is convenient to use the Jones matrix formalism. The transmission function of the PBOVL has the expression

$$\boldsymbol{T}(r,\varphi) = \cos\left(\frac{\Gamma}{2}\right) - i\sin\left(\frac{\Gamma}{2}\right) \times \begin{Bmatrix} \cos[2\alpha(r,\varphi)] & \sin[2\alpha(r,\varphi)] \\ \sin[2\alpha(r,\varphi)] & -\cos[2\alpha(r,\varphi)] \end{Bmatrix}, \tag{2}$$

where Γ is the optical phase retardation. The PBOVL is designed such that the birefringent film satisfies the half-wave-plate (HWP) condition, i.e., $\Gamma = \pi$, in order to maximize the coupling efficiency between SAM and OAM [18].

Here, we consider that the incident light is circularly polarized, as described by the Jones vector $\boldsymbol{E}_{\text{in}} = \boldsymbol{E}_0(r)|\pm\rangle$, with $|+\rangle = (1/\sqrt{2})[1\ i]^T$ and $|-\rangle = (1/\sqrt{2})[1\ -i]^T$ denoting the LHC and RHC polarization states, respectively. Under paraxial approximation, the modulated field just after the PBOVL can be expressed as

$$\begin{aligned}\boldsymbol{E}_{\text{out}}(r,\varphi) &= \boldsymbol{T}(r,\varphi)\boldsymbol{E}_{\text{in}} \\ &= -i\boldsymbol{E}_0(r)\exp\left[\pm i\left(2Q\varphi + \frac{\pi}{f\lambda}r^2 + 2\alpha_0\right)\right]|\mp\rangle,\end{aligned} \tag{3}$$

where the argument inside the complex exponential is the PB phase. The PB phase depends on the path trajectory on the Poincaré sphere that describes the evolution of polarization state of the incident light and is independent of the optical path length [24,25]. The $\pm$ sign of the PB-phase argument in Eq. (3) implies that the PBOVL has a remarkable polarization-dependent property of behaving as a convex (concave) lens with focal length $+f$ $(-f)$ when the incident light is RHC (LHC) polarized. Moreover, the RHC input beam is converted to a LHC focused vortex beam at the output with $-2Q\hbar$ OAM per photon, as shown in Fig. 1(a), while the LHC incident beam is converted to a defocused RHC vortex beam with the opposite OAM of $+2Q\hbar$, as illustrated in Fig. 1(b). Thus, the SAM and OAM of light are coupled to one another at the output of the PBOVL (i.e., the LHC is associated with the $-2Q\hbar$ OAM at the output and vice versa). The coupling between the SAM and OAM states of the modulated light can be understood based on the exchange of angular momentum from the light-matter interaction between the incident photon and the PBOVL [18].

The intensity profile of the output vortex beam at the observation screen situated at distance $z - z_0$ from the PBOVL can be deduced using the Fresnel-Kirchoff diffraction formula [26],

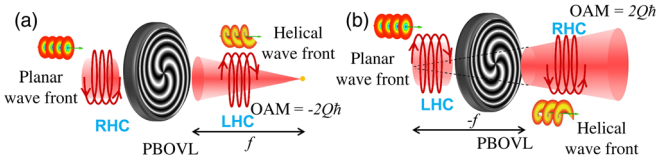

FIG. 1. Coupling of SAM-OAM states at the output of the PBOVL. Different OAM states at the output can be sorted by the bifocality of the PBOVL. (a) For the RHC-polarized incident wave, each photon of the focusing output wave possesses an OAM of $-2Q\hbar$ and is LHC polarized with a corresponding SAM of $+\hbar$. (b) For LHC-polarized incident wave, each photon of the defocusing output wave possesses an OAM of $+2Q\hbar$ and is RHC polarized with a corresponding SAM of $-\hbar$.

$$\boldsymbol{E}_{\text{out}}(\rho,\theta,z) = \frac{ik}{2\pi(z-z_0)}\exp\left(-ik\left[(z-z_0)+\frac{\rho^2}{2(z-z_0)}\right]\right) \times \int_0^{\infty}\int_0^{2\pi}\left\{\boldsymbol{E}_{\text{out}}(r,\varphi)\exp\left[-i\frac{k}{2}\left(\frac{r^2}{z-z_0}-\frac{2r\rho\cos(\varphi-\theta)}{z-z_0}\right)\right]\right\} r dr d\varphi, \tag{4}$$

where ρ and θ are the radial distance and azimuth angle at the observation screen, respectively. The incident light is considered as a collimated Gaussian beam, i.e., $\boldsymbol{E_0}(r) = e^{-r^2/w_0}$ in Eq. (3), where w_0 is the beam waist. Solving Eq. (4), the corresponding output intensity pattern for the RHC incident collimated light at various $z - z_0$ distances from the PBOVL, i.e., $S_{\text{out}}(\rho,\theta,z;|-\rangle) \propto |\boldsymbol{E}_{\text{out}}(\rho,\theta,z;|-\rangle)|^2$, can be expressed as

$$S_{\text{out}}(\rho,\theta,z;|-\rangle) \propto \left|\frac{-ik\rho^2 X[q(0)]\pi}{8(z-z_0)^2}\right|\left|\frac{X[q(0)]}{(z-z_0)}\right|^2\left|\exp\left(\frac{-ik\rho^2 X[q(0)]}{4(z-z_0)^2}\right)\right|^2 \times \left|I_{(|Q|-1/2)}\left(\frac{-ik\rho^2 X[q(0)]}{4(z-z_0)^2}\right) - I_{(|Q|+1/2)}\left(\frac{-ik\rho^2 X[q(0)]}{4(z-z_0)^2}\right)\right|^2, \tag{5}$$

where $1/X[q(0)] = 1/q(0) + 1/(z-z_0) - 1/f$, $q(0) = i\pi {w_0}^2/\lambda$, and $I_n(x)$ is the nth-order modified Bessel function. Similar for a collimated input LHC Gaussian beam, i.e., $S_{\text{out}}(\rho,\theta,z;|+\rangle) \propto |\boldsymbol{E}_{\text{out}}(\rho,\theta,z;|+\rangle)|^2$, the corresponding intensity profile can be expressed as

$$S_{\text{out}}(\rho,\theta,z;|+\rangle) \propto \left|\frac{-ik\rho^2 Y[q(0)]\pi}{8(z-z_0)^2}\right|\left|\frac{Y[q(0)]}{(z-z_0)}\right|^2\left|\exp\left(\frac{-ik\rho^2 Y[q(0)]}{4(z-z_0)^2}\right)\right|^2 \times \left|I_{(|Q|-1/2)}\left(\frac{-ik\rho^2 Y[q(0)]}{4(z-z_0)^2}\right) - I_{(|Q|+1/2)}\left(\frac{-ik\rho^2 Y[q(0)]}{4(z-z_0)^2}\right)\right|^2, \tag{6}$$

where $1/Y[q(0)] = 1/q(0) + 1/(z-z_0) + 1/f$. The close-form mathematical descriptions in Eqs. (5) and (6) are the important results deduced from the theoretical model, and the details of the derivation of these expressions are provided in Sec. I of the Supplemental Material [27]. The solutions give valuable insight into the understanding of the functionalities of the PBOVL by depicting various parameters (i.e., the Q value of the PBOVL) that govern the trends and optical response of the PBOVL.

III. FABRICATION VIA THE PANCHARATNAM-BERRY-PHASE POLARIZATION HOLOGRAM

Photonic devices operating in the visible spectrum are particularly attractive because the characteristics of the device can be directly observed by the human eye, and such devices can be applied in high-data-rate visible-light communication systems. Therefore, in this work, liquid-crystal polymer (LCP) is selected as the thin-film dielectric material for the realization of the PBOVL because of its high transmission in the visible spectrum while exhibiting good thermal and photochemical stability [28]. The LCP PBOVL is fabricated using photoalignment and PB-phase polarization holography technology. In order to control the optics axis orientation of the PBOVL, a polarization photosensitive alignment sulphonic azo-dye (SD1) layer is spin coated onto the substrate. Under exposure from a polarized light source in the UV-to-blue spectrum, the SD1 molecule tends to orient perpendicularly to the polarization of the incident light [28,29].

Figure 2 shows the optical setup for the PB-phase polarization hologram that is employed for realizing the PBOVL. The setup comprises a linear polarizer,

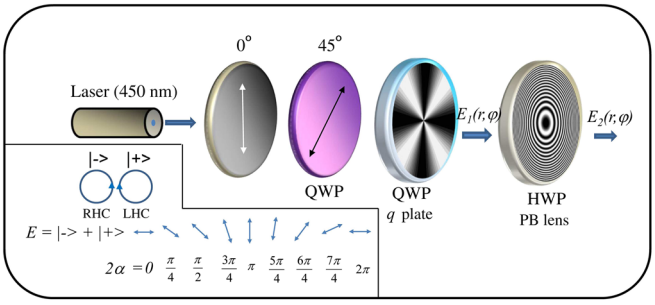

FIG. 2. Optical setup of PB-phase polarization hologram for establishing the optics axis orientation for the PBOVL. Inset diagram illustrates the dependence between the phase difference of the interfered orthogonal circularly polarized beams and the polarization direction of linearly polarized light.

a quarter-wave plate (QWP) with its optics oriented at 45° with respect to the transmission axis of the linear polarizer, followed by the LCP thin-film q plate and the PB-phase lens. The angular spatial distribution of the optics axis for the q plate is $\alpha_Q(\varphi) = Q\varphi + \alpha_0$ [18], while the optics axis distribution of the PB-phase lens is $\alpha_L(r) = \pi r^2/2f_L\lambda$, where f_L is the focal length of the PB lens [30]. The q plates with $Q = 1, 2, 4$ are realized using the rotational photoalignment setup as proposed in Ref. [31], while the PB-phase lens with focal length of 42 cm at 633 nm is fabricated using the polarization converter approach in Ref. [32].

The essence of the optical setup is to encrypt the desired optics axis distribution into the polarization angle of the linearly polarized light indicated by Eq. (1). Two orthogonal copropagating circularly polarized beams are generated from a single linearly polarized incident beam by the QWP oriented at 45° with respect to the transmission axis of the linear polarizer in Fig. 2. The phase offsets between the orthogonal circularly polarized beams are established from the PB-phase profile of the q plate and the PB lens. This differentiates from the conventional polarization hologram in Ref. [33], for which the phase difference is generated from the differences in the optical path length. According to the theory of polarization holography, the interference of two orthogonal circularly polarized beams gives the linearly polarized beam vibrating in a direction governed by the phase difference of these beams, as shown in the inset of Fig. 2. Using the Jones matrix analysis in Eq. (2), the Jones vector representation at the output is deduced to be

$$\begin{aligned}\boldsymbol{E_2}(r,\varphi) &= \boldsymbol{T_L}(r)\boldsymbol{E}_1(\varphi)\\ &= \frac{-1}{\sqrt{2}}\left(ie^{-i2\alpha_L(r)}|+\rangle + e^{i2\alpha_Q(\varphi)}e^{i2\alpha_L(r)}|-\rangle\right)\\ &= e^{-i[\alpha_Q(\varphi)+\pi/4]}\left\{\begin{array}{c}\cos[\alpha_Q(\varphi)+2\alpha_L(r)-\pi/4]\\ \sin[\alpha_Q(\varphi)+2\alpha_L(r)-\pi/4]\end{array}\right\}.\end{aligned} \tag{7}$$

The complex exponentials in Eq. (7) are the PB phases established between the interaction of light and the PBOE in Fig. 2. A detailed derivation of Eq. (7) is presented in Sec. II of the Supplemental Material [27].

Given the inhomogeneous linear polarization orientations in Eq. (7), the recorded profile on the polarization-sensitive SD1 alignment layer after a 150-s exposure from the 0.3-W/cm^2 450-nm laser is expressed as

$$\begin{aligned}\alpha_{\mathrm{SD1}}(r,\varphi) &= \alpha_Q(\varphi) + 2\alpha_L(r) - \frac{\pi}{4} + \frac{\pi}{2}\\ &= Q\varphi + \pi r^2/2(f_L/2)\lambda + \alpha_0 + \frac{\pi}{4}.\end{aligned} \tag{8}$$

A comparison of Eqs. (8) and (1) shows the fabricated PBOVL has the same Q value as the q plate, while the focal distance is 2 times shorter than the original PB lens. Subsequently, the UV-curable LCP layer is spin coated on top of the SD1 layer. The LCP material used is UCL017 (provided by Dainippon Ink and Chemicals) with a measured optical birefringence of 0.2 at 633 nm. The spin-coating speed is adjusted so that the approximately 1.6-μm optical thin-film PBOVL satisfies the HWP condition at 633 nm. A thermally stable micrometer thin film with optics axis distributed in the form of Eq. (1) is established after a photopolymerization process under a 5-min UV exposure.

Thus, the PBOVL can be realized economically from the PB-phase hologram using a simple optical setup presented in Fig. 2 and efficiently as the device can be realized under a single-step exposure. The advantages of this method outweigh the sophisticated and time-consuming optical approach using the digital mechanical mirror system in Refs. [19,20,34]. Moreover, in this work, we apply the physics of the PB-phase hologram for the realization of an optical element. It should be emphasized that this method is not limited to the realization of the PBOVL and can be generalized to the fabrication of other PBOEs for which FPG can be realized by changing the HWP PB lens to HWP polarization grating.

IV. RESULTS

The optics axis alignment of the fabricated thin-film dielectric PBOVL can be evaluated under a polarization microscope. The top row of Fig. 3(a) shows the polarization micrographs of the fabricated PBOVL samples with $Q = 1$, 2, and 4, all of which have a focal distance of 21 cm at 633 nm and an aperture size of 10 mm. The observation from the polarization micrographs shows a series of consecutive bright and dark fringes spiraling in the counterclockwise direction for positive Q towards the phase singularity at the center. The bright (dark) fringes correspond to the local polarization direction of output light approaching the transmission axis of the analyzer in the parallel (orthogonal) directions, respectively. Since the polarization state is modulated as a result of the inhomogeneous optics axis distribution of the PBOVL, the number of fringes increases in the φ direction for the PBOVL with greater Q. This fringe increment is due to the increase in the rate of change in the optics axis orientation, as depicted in the φ dependence of Eq. (1). Similarly, the width of the fringes gradually decreases away from the center since the rate of change of the optics axis increases with r. A smooth change in the gray levels between each successive bright and dark fringe in the micrographs indicates a gradual change in the alignment orientation of the fabricated PBOVL samples. The polarization interference patterns from the micrographs are in good agreement with the simulations shown in the bottom row of Fig. 3(a).

The operational characteristics of the fabricated PBOVL are tested from the experimental setup shown in Fig. 3(b).

The experimental setup consists of a 633-nm helium neon laser source illuminating the beam towards the beam expander establishing a collimated beam with a beam diameter of around 15 mm. The expanded Gaussian beam is fed to the linear polarizer, which is subsequently followed by a QWP converting the beam to the LHC-polarized state. The LC HWP modulates the polarization between the LHC and RHC states, followed by a 5-mm circular aperture located in front of the tested PBOVL sample to ensure the beam diameter is within the aperture size of the PBOVL. Finally, the diffraction pattern of the PBOVL is captured from the CMOS camera.

In the absence of applied voltage across the LC HWP, the incident beam passing through the PBOVL is RHC polarized. A LHC-polarized focused vortex beam with OAM of $-2Q\hbar$ is generated at the output, which corresponds to the scenario depicted in Fig. 1(a). Conversely, when a 5-V 1-kHz square-wave ac signal is applied across the LC HWP, the polarization of incident light is unmodulated and remains LHC polarized. In this circumstance, the PBOVL behaves as a concave lens and establishes a defocused RHC-polarized vortex beam with OAM of $2Q\hbar$ at the output, which corresponds to the case in Fig. 1(b).

The diffraction pattern of the PBOVL with $Q = 1, 2, 4$ and $f = 21$ cm for various output states is shown in Fig. 3(c). The diagrams on the top and bottom rows in Fig. 3(c) represent the diffraction intensity profile of the focused and defocused states, respectively. Both focused and defocused states show the expected annular intensity diffraction pattern of the vortex beam. All diffraction patterns in Fig. 3(c) are captured by the CMOS camera located 15 cm from the PBOVL. The selected location of the camera ensures that the size of the vortex core corresponding to the dark region at the center can be clearly captured by the limited resolution of the camera, while the focused and defocused states can be clearly distinguished from the intensity and beam-size contrast. Furthermore, the selected distance avoids saturation in the brightness of the focused state when the international standard organization (ISO) sensitivity of the CMOS camera is set to its lowest possible value (ISO 100). Thus, the actual intensity contrast between the focused and defocused states is, in fact, much higher than the diagrams illustrated in Fig. 3(c), as the camera sensor for the defocused state is set to be 8 times more sensitive (ISO 800) than the focused state (ISO 100). In addition, the actual size of the laser spot for the focused state is several times smaller than the defocused state, as the scales between the focused and defocused states are different in Fig. 3(c).

By removing the QWP from the system in Fig. 3(b), the incident light at the PBOVL becomes linearly polarized, and the corresponding diffraction pattern is shown in Fig. 3(d). The diffraction pattern for both focused and defocused states from the PBOVL with $Q = 2$ appears simultaneously in Fig. 3(d) because a linearly polarized light can be decomposed into LHC and RHC incident light. The photograph captured in Fig. 3(d) is captured with the camera sensitivity

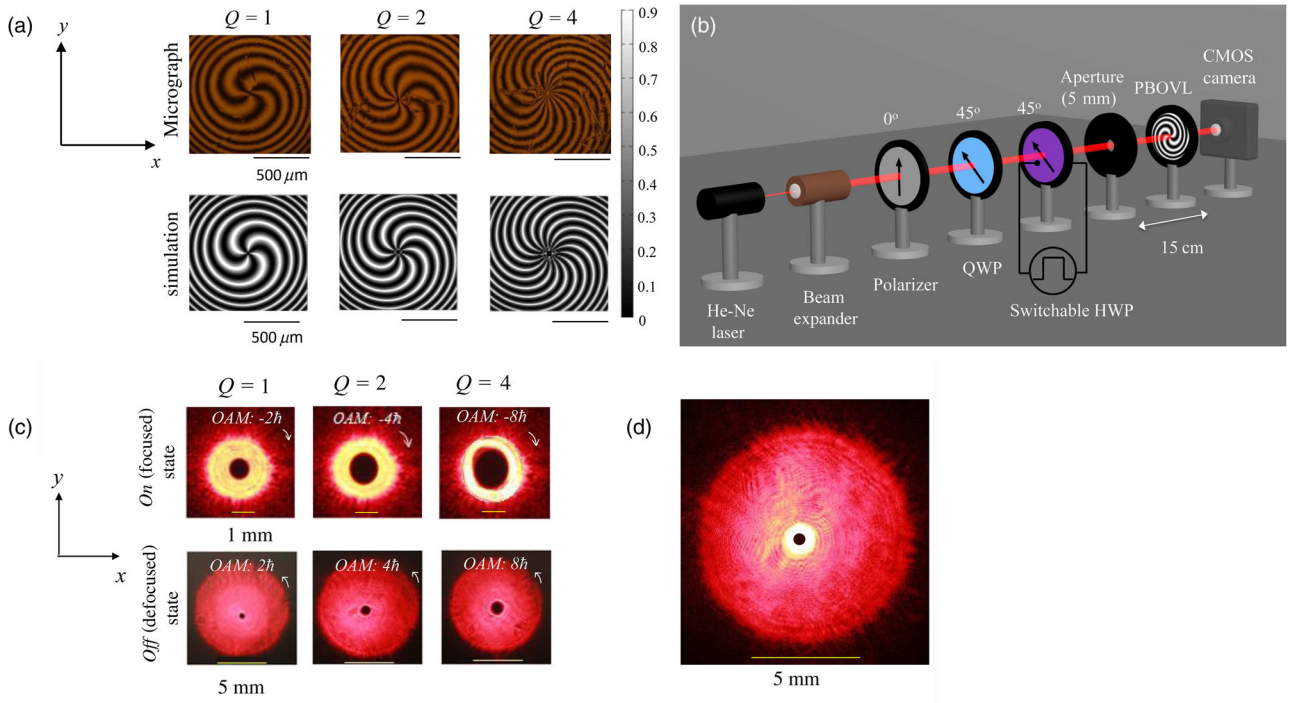

Fig. 3. (*Continued*).

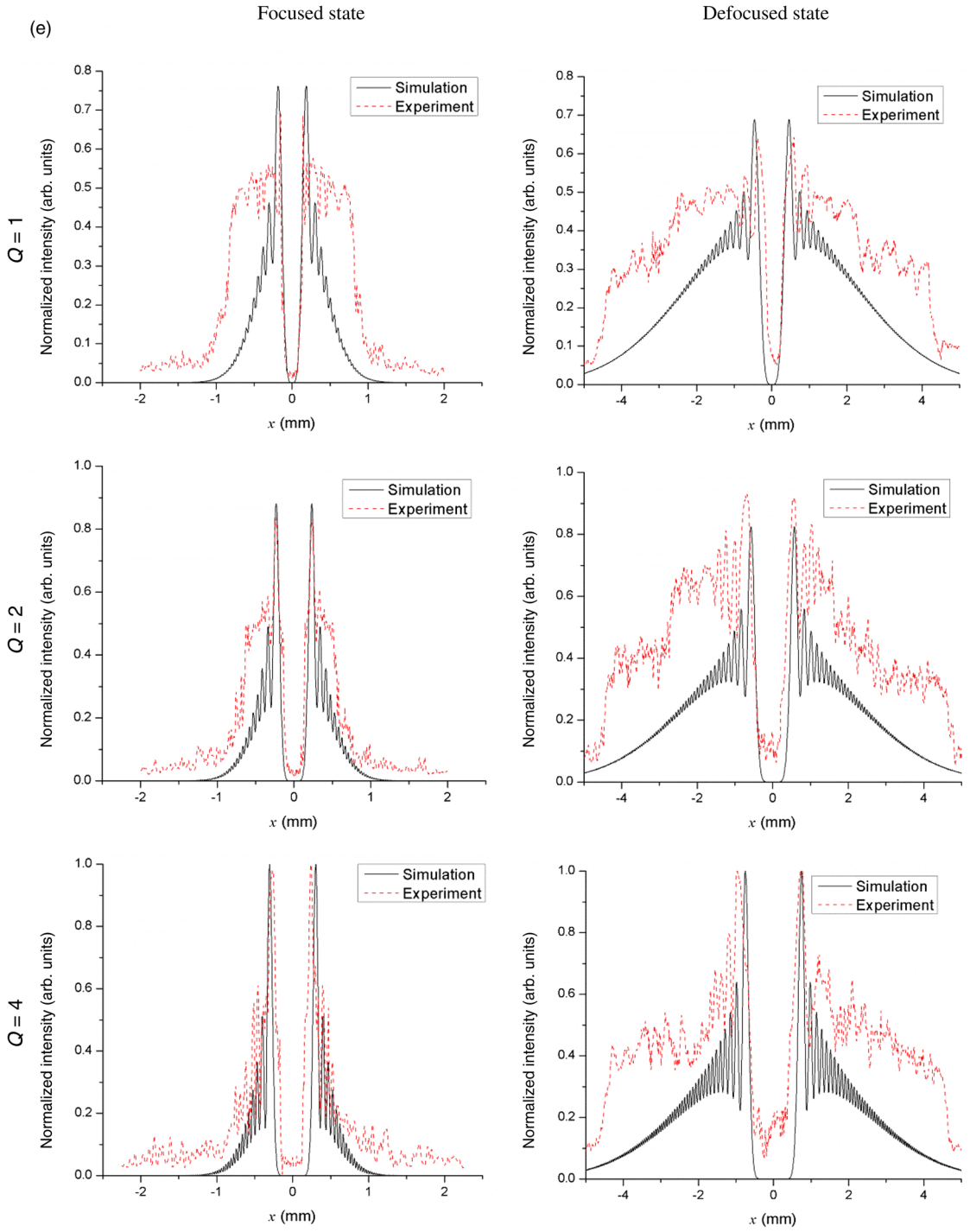

FIG. 3. Experimental demonstration of establishing a bifocal vortex system from the fabricated PBOVL. (a) Transmittance profile of the PBOVL captured under crossed polarizers. The micrograph of the samples for $Q = 1, 2, 4$ with $f = 21$ cm are shown in the top row, and their corresponding simulated profile is shown in the bottom row. Line scale represents 500 μm. Gray-scale bar indicates the intensity of the simulation. (b) Experimental setup for realizing a bifocal vortex system using the PBOVL. The liquid-crystal HWP behaves as a polarization switch selecting a focusing (defocusing) LHC- (RHC-) polarized output wave with an OAM of $-2Q\hbar$ ($2Q\hbar$) in the voltage *off* (*on*) state. (c) The diffraction pattern of the optical beam captured by CMOS camera (Canon EOS 600D). Top (bottom) row corresponds to the intensity pattern of the focused (defocused) vortex beam from the $Q = 1, 2, 4$ PBOVL captured with ISO sensitivity of 100 (800) for the RHC (LHC) incident Gaussian beam. Line scale for the focused and defocused states is 1 and 5 mm, respectively. (d) The diffraction pattern for the linearly polarized Gaussian incident beam from the $Q = 2$ PBOVL. (e) Comparison of the intensity profile between simulated (black solid line) and experimental results (red dashed line). Intensity for focused and defocused states are normalized with respect to the maximum intensity of the PBOVL with $Q = 4$ to their corresponding states, respectively. The origin is taken at the center of the vortex beam.

adjusted at ISO 800, for which the saturated bright tiny annular ring at the center corresponds to the focused state, while the surrounding red region corresponds to the contribution from the defocused state. Thus, two focal points appear simultaneously at the output for an incident beam with an arbitrary polarization state. Different circularly polarized components coupled to the $+2$ (-2) Q OAM state can be spatially distinguished by the bifocality of the PBOVL. In the special case of circularly polarized incident light, only one focal point appears where the focal distance and OAM are governed by the handedness of the circular polarization (spin). By locating a photodetector directly at the output of the PBOVL, the optical throughput of various output states is measured to be as high as 90%. The losses are primarily due to the index mismatch between air-glass interfaces at the PBOVL substrate. In addition, the measured first-order diffraction efficiency, which depicts the conversion efficiency of the SAM-to-OAM conversion of the device, is as high as 91%. The inability to establish full SAM-to-OAM conversion, i.e., 100% diffraction efficiency, can be explained by the slight mismatch between the operating wavelength of the fabricated PBOVL and the wavelength of the incident light.

By comparing the diffraction pattern of the PBOVL with different Q for the focused and defocused states in Fig. 3(c), we observe that the size of the vortex core and the intensity of the bright annular ring increase for the PBOVL with greater Q. In addition, the width of the bright annular ring decreases for the PBOVL with greater Q. In fact, such trends are predicted in Sec. II. Figure 3(e) provides a direct comparison between the simulated intensity profile and the measured intensity profile taken from the x axis that passes through the center of the vortex beam. The plots of the simulation results for the focused and defocused states are derived using Eqs. (5) and (6), respectively. The simulation parameters are provided in Table S1 in the Supplemental Material [27]. The intensity profiles of the focused and defocused states for the PBOVL with $Q = 1$, 2, and 4 in Fig. 3(e) are normalized with respect to the intensity maxima of $Q = 4$ to their corresponding state, respectively. Figure 3(e) shows that the simulated results are in good agreement with the experimental results near the center region of the intensity profile. Farther away from the center of the vortex beam, a rapid decay of the intensity profile appears in the experimental results that are not depicted in the simulation. This can be explained by the presence of the 5-mm aperture in the setup in Fig. 3(b) that reduces the size of the incident beam and is not accounted for in the simulation model.

V. DISCUSSION

A. Sorting of nonseparable SAM and OAM output states

In the general case for which the incident light is arbitrarily polarized, the focused beam carrying $-2Q\hbar$ OAM and $+\hbar$ SAM and the defocused beam carrying $+2Q\hbar$ OAM and $-\hbar$ SAM are superimposed at the output [see Fig. 3(d) for the case of linear polarized light]. The corresponding quantum-mechanical representation of the photon output state takes the form

$$|\psi_{\text{out}}\rangle = \chi\sqrt{S_{\text{out}}(\rho,\theta,z;|-\rangle)}|+\rangle|-2Q\rangle + \gamma\sqrt{S_{\text{out}}(\rho,\theta,z;|+\rangle)}|-\rangle|2Q\rangle, \quad (9)$$

where $S_{\text{out}}(\rho,\theta,z;|-\rangle)$ and $S_{\text{out}}(\rho,\theta,z;|+\rangle)$ are the intensity profiles of the output diffracted wave with the expression given in Eqs. (5) and (6), respectively. The state vector $|2Q\rangle = \exp(i2Q\hbar)$ is the shorthand notation of the OAM state with topological charge $2Q$. The complex coefficients χ and γ are dependent on the polarization state of incident light and satisfy the normalized condition $|\chi|^2 + |\gamma|^2 = 1$. It is clear from Eq. (9) that the OAM and SAM photon states are correlated and, hence, nonseparable. In the scenario of a linearly polarized incident light, we have $\chi = \gamma = 1/\sqrt{2}$ corresponding to the mathematical form of the Bell state [35]. In the special case of a circularly polarized incident wave, we have $\chi = 1, \gamma = 0$ and $\chi = 0, \gamma = 1$ for LHC and RHC waves, respectively, for which only one coupled SAM and OAM component appears (either the first or second term for the RHC (LHC) input, respectively) in Eq. (9). Since $S_{\text{out}}(\rho,\theta,z;|-\rangle)$ and $S_{\text{out}}(\rho,\theta,z;|+\rangle)$ take a different expression, this intensity difference implies that a photon associated with a different OAM can be spatially sorted at the output of the PBOVL. Although Fig. 3(d) shows some intensity overlapping between the two focal states, where each focal state is associated with the same magnitude but opposite SAM and OAM, at the focal plane (21 cm from the PBOVL, i.e., $z - z_0 = 21$ cm), the overlapping is significantly reduced. In fact, the focused vortex beam passes through the dark vortex core of the defocused beam, and this can be easily verified by Eqs. (5) and (6). Thus, locating a circular millimeter-size aperture at the focal plane can effectively remove the defocused RHC component with an OAM of $2Q\hbar$. The nonseparable SAM and OAM states and the capability to sort these coupled components can be useful for enhancing the performance of the ququart receiver presented in Refs. [36,37].

B. Implications for optical manipulation

The features of the PBOVL including bifocality and the capability to generate OAM with different handedness at each focal point are particularly attractive in the application of optical trapping, as it provides the possibility of twist deformation in the optical trap. An optical trap can be realized when the optical gradient force is large enough to balance the light-scattering force and the weight of the trapped particle [38]. A large gradient force is established near the beam waist of the focal point. Therefore, in order to establish dual optical traps in the longitudinal direction using the PBOVL, it is vital to have two focal points with

positive focal length, and, thus, an additional objective lens is required to shift the negative focal length of the PBOVL to a positive value. Of course, this focal length adjustment requires the focal length of the objective lens to be much smaller than the focal length of the PBOVL, i.e., $f_L \ll f_{\mathrm{PBOVL}}$. The focal lengths of the bifocal system in Fig. 4 are deduced to be $f_\pm = f_L f_{\mathrm{PBOVL}}/(f_{\mathrm{PBOVL}} \pm f_L)$. In fact, dual optical trapping has demonstrated many fascinating phenomena such as examining mechanical deformation of red blood cells by dynamically adjusting the separation distance of the two closely spaced traps [39]. Similar action can be realized in a PBOVL system by dynamically switching in between two optical traps f_+ and f_-, provided the refreshing rate of the beam is much faster than the relaxation time of the trapped particle (0.1 s for red blood cells), for which the trapped particle feels the time-averaged effect of both traps [39]. Fast switching between f_+ and f_- can be easily performed from a LC HWP modulating between the RHC and LHC polarization states, as demonstrated in Fig. 3(b). Moreover, such phenomenon also requires the separation distance of the traps, i.e., $\Delta f = f_+ - f_-$, to be smaller than the axial length of the trapped particles so that the particle will be influenced by the actions of both traps. Since the dual optical traps generated from a PBOVL system exhibit equal but opposite OAM, both ends of the trapped particle will, thus, experience different torque. This torque difference leads to an interesting action known as the optical twist, as shown in Fig. 4. The twisting action provided from the OAM beam can be extremely useful in biological studies such as the examination of the mechanical behavior of various biological samples, i.e., DNA, and the manipulation in nanomachines as well as nanofabrication.

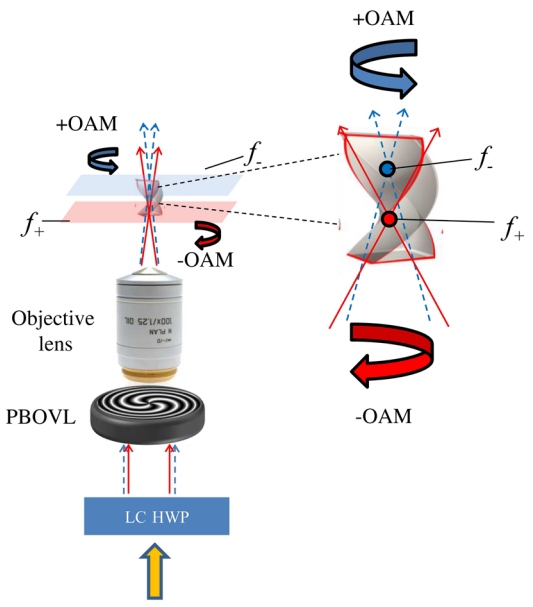

FIG. 4. Illustration of the realization of the optical twist from the proposed PBOVL system. Two closely spaced traps with equal and opposite OAM are switched at a rate faster than the relaxation time of the trapped particle. The trapped particle feels the time-averaged effect of both traps and, thus, is stretched and twisted by the optical stresses from both traps.

C. Implications for OAM lasing

The developed PBOVL can be applied for the realization of an OAM laser. An OAM laser consists of a laser cavity that generates a coherent helical beam with definite OAM of $Q\hbar$ per photon. However, it is usually difficult to generate a helical light beam directly from the laser cavity using a conventional OAM generator, such as a q plate, due to the simultaneous generation of helical modes with opposite azimuthal handedness $[-Q\ (+Q)]$ and the inability to distinguish these modes as they exhibit the same spatial intensity distribution, identical radii of curvature with equal path length, and identical Gouy phase shift. An OAM laser has been experimentally demonstrated using a q plate [40]. However, the configuration proposed in Ref. [40] is complicated and involves many optical components such as polarization beam splitters and many birefringent wave plates. Thus, the laser design in Ref. [40] is space consuming with relatively low gain due to a vast number of optical components inside the optical cavity. The coupling between the SAM and OAM of light as well as the ability to spatially distinguish these components from the properties of the PBOVL are crucial for the realization of an OAM laser. Figure 5 illustrates our simple proposed scheme for the realization of a laser cavity generating a helical beam with definite OAM for a He-Ne laser using the PBOVL. A high-voltage pulse is initially applied in the He-Ne tube to create population inversion, and, thus, inside the gain medium, two orthogonal polarization lasing modes are established, which correspond to the red and blue tracing rays, respectively, in Fig. 5. The table in Fig. 5 specifies the changes in OAM and the state of polarization (SOP) of the red and blue tracing rays after

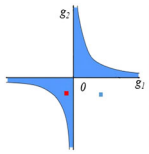

Optical Components	Incident Ray				Output Ray			
	Ray (Red)		Ray (Blue)		Ray (Red)		Ray (Blue)	
	SOP	OAM	SOP	OAM	SOP	OAM	SOP	OAM
PBOVL (+z)	*RHC*	*0*	*LHC*	*0*	*LHC*	*-2Qħ*	*RHC*	*2Qħ*
Mirror	*LHC*	*-2Qħ*	*RHC*	*2Qħ*	*RHC*	*2Qħ*	*LHC*	*-2Qħ*
PBOVL (-z)	*RHC*	*2Qħ*	*LHC*	*-2Qħ*	*LHC*	*0*	*RHC*	*0*

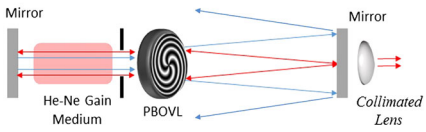

FIG. 5. Proposed configuration for realization of an OAM laser using the PBOVL. The red tracing rays denote the helical mode that is within the laser stability criterion region for which lasing occurs, while the blue tracing rays denote the orthogonal helical mode which does not satisfy the stability criterion, and, thus, no lasing occurs. Inset table shows the incident and output state of the orthogonal modes at various optical elements inside the cavity.

interacting with the optical elements inside the cavity. When both polarization lasing modes pass through the PBOVL in the $+z$ direction, the polarization state of the incident LHC (RHC) wave will be converted to a RHC (LHC) wave gaining an OAM of -2 $(+2)$ $Q\hbar$ and is sorted by the focal distance $+f_1$ $(-f_1)$ at the output, as shown by the red (blue) tracing rays in Fig. 5. Because of mirror symmetry, the handedness of the circular polarization and the OAM state of the reflected rays are reversed, as shown from the table in Fig. 5. Since the response of the PBOVL is polarization nonreciprocal, the red and blue tracing rays, thus, lose an OAM of -2 $(+2)$ $Q\hbar$ as they transverse pass the PBOVL in the $-z$ direction, as indicated by the table in Fig. 5. The laser cavity in Fig. 5 is designed such that the polarization states and the spatial modes are the same after each complete round-trip. Moreover, the focal distances of both PBOVLs are designed such that the $-2Q$ mode with $-2Q\hbar$ OAM that corresponds to the red tracing rays is within the region of the laser stability criterion (inside the blue region in the graph of Fig. 5). The stability criterion is given by $0 \leq (1 - L/R_1)(1 - L/R_2) \leq 1$, where L is the length of the cavity, and R_1 and R_2 are the effective radii of the curvature of the PBOVL and the reflecting mirror, respectively. Therefore, the mode corresponding to the red tracing rays is self-sustained, and a portion of the coherent beam will leak through the partially reflecting mirror causing the laser to lase at 633 nm with $-2Q\hbar$ OAM and is RHC polarized. Conversely, due to the mode distinguishability of the PBOVL, the $+2Q$ mode that is represented by the blue tracing ray does not satisfy the laser stability criterion, and, thus, lasing will not occur for this mode.

VI. CONCLUSIONS

In summary, we present the properties of the thin-film dielectric PBOVL experimentally and deduce mathematical close-form expressions that provide theoretical descriptions for these behaviors. The physics of PB-phase holography is discussed and applied in the realization of the PBOVL. Through the generation of a vortex beam, the SAM and OAM states are classically nonseparable at the output of the PBOVL, and coupled states with different spin can be sorted by the bifocality of the lens. The theoretical model of the PBOVL is established using Fresnel-Kirchoff diffraction theory and is in good agreement with the experimental result. The LCP PBOVL is realized using our optical setup operating under the principle of the PB-phase hologram. We discuss that the characteristics of the PBOVL can be useful in the generation of optical twist in a bifocal optical-vortex trapping system as well as the realization of an OAM laser. Therefore, the features of the PBOVL have great potential to become an important tool in the community of physics and engineering that may find applications in biological studies, optical rotor design, quantum-information processing, and theoretical physics.

ACKNOWLEDGMENTS

We acknowledge Dr. Kerry Hinton from the University of Melbourne for his fruitful discussions about quantum optics. This work is supported by the Research Grants Council, Hong Kong Government through the Theme-Based Research Project under Grant No. T23-713/11-1. This work is partially supported by the National Natural Science Foundation of China (Grants No. 61605046 and No. 11574079) and Fundamental Research Funds for the Central Universities of China.

A. M. W. T., F. F., and T. D. contributed equally to this work.

[1] L. Allen, M. W. Beijersbergen, R. J. C. Spreeuw, and J. P. Woerdman, Orbital angular momentum of light and the transformation of Laguerre-Gaussian laser modes, Phys. Rev. A **45**, 8185 (1992).

[2] J. Poynting, The wave motion of a revolving shaft, and a suggestion as to the angular momentum in a beam of circularly polarized light, Proc. R. Soc. A **82**, 560 (1909).

[3] G. Molina-Terriza, J. P. Torres, and L. Torner, Twisted photons, Nat. Phys. **3**, 305 (2007).

[4] G. A. Swartzlander, E. L. Ford, R. S. Abdul-Malik, L. M. Close, M. A. Peters, D. M. Palacios, and D. W. Wilson, Astronomical demonstration of an optical vortex coronagraph, Opt. Express **16**, 10200 (2008).

[5] C. Zhang, K. Wang, J. Bai, S. Wang, W. Zhao, F. Yang, C. Gu, and G. Wang, Nanopillar array with a $\lambda/11$ diameter fabricated by a kind of visible CW laser direct lithography system, Nanoscale Res. Lett. **8**, 280 (2013).

[6] J. Wang, J. Y. Yang, I. M. Fazal, N. Ahmed, Y. Yan, H. Huang, Y. Ren, Y. Yue, S. Dolinar, M. Tur, and A. E. Willner, Terabit free-space data transmission employing orbital angular momentum multiplexing, Nat. Photonics **6**, 488 (2012).

[7] G. Berkhout, M. Lavery, J. Courtial, M. Beijersbergen, and M. J. Padgett, Efficient Sorting of Orbital Angular Momentum States of Light, Phys. Rev. Lett. **105**, 153601 (2010).

[8] W. Zhang, Q. Qi, J. Zhou, and L. Chen, Mimicking Faraday Rotation to Sort the Orbital Angular Momentum of Light, Phys. Rev. Lett. **112**, 153601 (2014).

[9] S. Li and J. Wang, Simultaneous demultiplexing and steering of multiple orbital angular momentum modes, Sci. Rep. **5**, 15406 (2015).

[10] T. Lei, M. Zhang, Y. Li, P. Jia, G. N. Liu, X. Xu, Z. Li, C. Min, J. Lin, C. Yu, H. Niu, and X. Yuan, Massive individual orbital angular momentum channels for multiplexing enabled by Dammann gratings, Light Sci. Appl. **4**, e257 (2015).

[11] M. Friese, J. Enger, H. Rubinsztein-Dunlop, and N. Heckenberg, Optical alignment and spinning of laser-trapped microscopic particles. Nature (London) **394**, 348 (1998).

[12] H. He, M. Friese, N. Heckenberg, and H. Rubinsztein-Dunlop, Direct Observation of Transfer of Angular Momentum to Absorptive Particles from a Laser Beam with a Phase Singularity, Phys. Rev. Lett. **75**, 826 (1995).

[13] M. Padgett and R. Bowmen, Tweezers with a twist, Nat. Photonics **5**, 343 (2011).
[14] S. Sato, M. Ishlgure, and H. Inaba, Optical trapping and rotational manipulation of microscopic particles and biological cells using higher-order mode Nd:YAG laser beams, Electron. Lett. **27**, 1831 (1991).
[15] J. W. R. Tobasa and D. V. Petrov, Optical Pumping of Orbital Angular Momentum of Light in Cold Cesium Atoms, Phys. Rev. Lett. **83**, 4967 (1999).
[16] H. Ukita and K. Nagatomi, Optical tweezers and fluid characteristics of an optical rotator with slopes on the surface upon which light is incident and a cylindrical body, Appl. Opt. **42**, 2708 (2003).
[17] M. W. Beijersbergen, R. P. C. Coerwinkel, M. Kristensen, and J. P. Woerdman, Helical-wavefront laser beams produced with a spiral phaseplate, Opt. Commun. **112**, 321 (1994).
[18] L. Marrucci, C. Manzo, and D. Paparo, Optical Spin-to-Orbital Angular Momentum Conversion in Inhomogeneous Anisotropic Media, Phys. Rev. Lett. **96**, 163905 (2006).
[19] B. Y. Wei, W. Hu, Y. Ming, F. Xu, S. Rubin, J. G. Wang, V. Chigrinov, and Y. Q. Lu, Generating switchable and reconfigurable optical vortices via photopatterning of liquid crystals, Adv. Mater. **26**, 1590 (2014).
[20] P. Chen, B. Y. Wei, W. Ji, S. J. Ge, W. Hu, F. Xu, V. Chigrinov, and Y. Q. Lu, Arbitrary and reconfigurable optical vortex generation: A high-efficiency technique using director-varying liquid crystal fork gratings, Photon. Res. **3**, 133 (2015).
[21] J. Leach, M. J. Padgett, S. M. Barnett, S. Franke-Arnold, and J. Courtial, Measuring the Orbital Angular Momentum of a Single Photon, Phys. Rev. Lett. **88**, 257901 (2002).
[22] G. C. G. Berkhout, M. P. J. Lavery, J. Courtial, M. Beijersbergen, and M. J. Padgett, Efficient Sorting of Orbital Angular Momentum States of Light, Phys. Rev. Lett. **105**, 153601 (2010).
[23] M. Mirhosseini, M. Malik, Z. Shi, and R. W. Boyd, Efficient separation of the orbital angular momentum eigenstates of light, Nat. Commun. **4**, 2781 (2013).
[24] S. Pancharatnam, Generalized theory of interference, and its applications Part I. Coherent pencils, Proc. Indian Acad. Sci. A **44**, 247 (1956).
[25] M. Berry, Quantal phase factors accompanying adiabatic changes, Proc. R. Soc. A **392**, 45 (1984).
[26] L. Janicijevic and S. Topuzoski, Fresnel and Fraunhofer diffraction of a Gaussian laser beam by fork-shaped gratings, J. Opt. Soc. Am. A **25**, 2659 (2008).
[27] See Supplemental Material at http://link.aps.org/supplemental/10.1103/PhysRevApplied.7.034010 for details of the mathematical derivation of the PBOVL intensity profile and calculation of the polarization state at PB-phase hologram output.
[28] T. Du, F. Fan, A. M. W. Tam, J. Sun, V. G. Chigrinov, and H. S. Kwok, Complex nanoscale-ordered liquid crystal polymer film for high transmittance holographic polarizer, Adv. Mater. **27**, 7191 (2015).
[29] V. Chigrinov, S. Pikin, A. Verevochnikov, V. Kozendov, M. Khazimullin, J. Ho, D. D. Huang, and H. S. Kwok, Diffusion model of photoaligning in azo-dye layers, Phys. Rev. E **69**, 061713 (2004).
[30] E. Hasman, V. Kleiner, G. Biener, and A. Niv, Polarization dependent focusing lens by use of quantized Pancharatnam-Berry phase diffractive optics, Appl. Phys. Lett. **82**, 328 (2003).
[31] S. Slussarenkko, A. Murauski, T. Du, V. Chigrinov, L. Marrucci, and E. Santamato, Tunable liquid crystal q-plates with arbitrary topological charge, Opt. Express **19**, 4085 (2011).
[32] A. M. W. Tam, F. Fan, H. S. Chen, D. Tao, V. G. Chigrinov, H. S. Kwok, and Y. H. Lin, "Continuous" nanoscale patterned photoalignment for thin film Pancharatnam-Berry phase diffractive lens, Proc. EuroDisplays **46**, 8 (2015).
[33] L. Nikolova and T. Todorov, Diffraction efficiency and selectivity of polarization holographic recording, Opt. Acta **31**, 579 (1984).
[34] P. Chen, S. Ge, L. Ma, W. Hu, V. G. Chigrinov, and Y. Lu, Generation of Equal-Energy Orbital Angular Momentum Beams via Photopatterned Liquid Crystals, Phys. Rev. Applied **5**, 044009 (2016).
[35] S. Straupe and S. Kulik, The quest for higher dimensionality, Nat. Photonics **4**, 585 (2010).
[36] E. Nagali, F. Sciarrino, F. D. Martini, L. Marrucci, B. Piccirillo, E. Karimi, and E. Santamato, Quantum Information Transfer from Spin to Orbital Angular Momentum of Photons, Phys. Rev. Lett. **103**, 013601 (2009).
[37] E. Nagali, L. Sansoni, L. Marrucci, E. Santamato, and F. Sciarrino, Experimental generation and characterization of single-photon hybrid ququarts based on polarization and orbital angular momentum encoding, Phys. Rev. A **81**, 052317 (2010).
[38] A. Ashkin, J. M. Dziedzic, J. E. Bjorkholm, and S. Chu, Observation of a single-beam gradient force optical trap for dielectric particles, Opt. Lett. **11**, 288 (1986).
[39] L. Yu and Y. Sheng, Mechanical analysis of the optical tweezers in time-sharing regime, Opt. Express **22**, 7953 (2014).
[40] D. Naidoo, F. S. Roux, A. Dudley, I. Litvin, B. Piccirillo, L. Marrucci, and A. Forbes, Controlled generation of higher-order Poincare sphere beams from a laser, Nat. Photonics **10**, 327 (2016).